

---

This is an electronic reprint of the original article.  
This reprint may differ from the original in pagination and typographic detail.

Sutter, P.; Komsa, H. P.; Krasheninnikov, A. V.; Huang, Yuan; Sutter, E.  
**Luminescence of defects in the structural transformation of layered tin dichalcogenides**

*Published in:*  
Applied Physics Letters

*DOI:*  
[10.1063/1.5007060](https://doi.org/10.1063/1.5007060)

Published: 25/12/2017

*Document Version*  
Publisher's PDF, also known as Version of record

*Please cite the original version:*  
Sutter, P., Komsa, H. P., Krasheninnikov, A. V., Huang, Y., & Sutter, E. (2017). Luminescence of defects in the structural transformation of layered tin dichalcogenides. *Applied Physics Letters*, 111(26), 1-5. Article 262102. <https://doi.org/10.1063/1.5007060>

---

This material is protected by copyright and other intellectual property rights, and duplication or sale of all or part of any of the repository collections is not permitted, except that material may be duplicated by you for your research use or educational purposes in electronic or print form. You must obtain permission for any other use. Electronic or print copies may not be offered, whether for sale or otherwise to anyone who is not an authorised user.

## Luminescence of defects in the structural transformation of layered tin dichalcogenides

P. Sutter, H.-P. Komsa, A. V. Krasheninnikov, Y. Huang, and E. Sutter

Citation: *Appl. Phys. Lett.* **111**, 262102 (2017); doi: 10.1063/1.5007060

View online: <https://doi.org/10.1063/1.5007060>

View Table of Contents: <http://aip.scitation.org/toc/apl/111/26>

Published by the [American Institute of Physics](#)

---

### Articles you may be interested in

[Burying non-radiative defects in InGaN underlayer to increase InGaN/GaN quantum well efficiency](#)  
*Applied Physics Letters* **111**, 262101 (2017); 10.1063/1.5007616

[Modulating PL and electronic structures of MoS<sub>2</sub>/graphene heterostructures via interlayer twisting angle](#)  
*Applied Physics Letters* **111**, 263106 (2017); 10.1063/1.5011120

[Structural and electron transport properties of single-crystalline In<sub>2</sub>O<sub>3</sub> films compensated by Ni acceptors](#)  
*Applied Physics Letters* **111**, 262103 (2017); 10.1063/1.5006421

[Temperature-dependent transport properties of graphene decorated by alkali metal adatoms \(Li, K\)](#)  
*Applied Physics Letters* **111**, 263502 (2017); 10.1063/1.5001080

[High transmittance contrast in amorphous to hexagonal phase of Ge<sub>2</sub>Sb<sub>2</sub>Te<sub>5</sub>: Reversible NIR-window](#)  
*Applied Physics Letters* **111**, 261102 (2017); 10.1063/1.5009610

[New signature discovered characterizes structural defects in tin dichalcogenides](#)  
*Scilight* **2017**, 270004 (2017); 10.1063/1.5020516

---

Quantum Design Brings You the Next Generation Magneto-Optic Cryostat



Only be limited by your imagination...

Room Temperature Window  
Split-Coil Conical Magnet  
Sample Pod  
User Wiring Ports

Learn More

Quantum Design  
qdusa.com/opticool5

8 Optical Access Ports: 7 Side; 1 Top  
Temperature Range: 1.7 K to 350 K  
7 T Split-Coil Conical Magnet  
Low Vibration: <10 nm peak-to-peak  
89 mm x 84 mm Sample Volume  
Automated Temperature & Magnet Control  
Cryogen Free

## Luminescence of defects in the structural transformation of layered tin dichalcogenides

P. Sutter,<sup>1(a)</sup> H.-P. Komsa,<sup>2</sup> A. V. Krasheninnikov,<sup>2,3,4</sup> Y. Huang,<sup>5</sup> and E. Sutter<sup>6</sup>

<sup>1</sup>Department of Electrical and Computer Engineering, University of Nebraska-Lincoln, Lincoln, Nebraska 68588, USA

<sup>2</sup>Department of Applied Physics, Aalto University, P.O. Box 11100, FI-00076 Aalto, Finland

<sup>3</sup>Institute of Ion Beam Physics and Materials Research, Helmholtz-Zentrum Dresden-Rossendorf, 01314 Dresden, Germany

<sup>4</sup>National University of Science and Technology MISiS, 119049 Moscow, Russia

<sup>5</sup>Beijing National Laboratory for Condensed Matter Physics, Institute of Physics, Chinese Academy of Sciences, Beijing 100190, People's Republic of China

<sup>6</sup>Department of Mechanical and Materials Engineering, University of Nebraska-Lincoln, Lincoln, Nebraska 68588, USA

(Received 29 September 2017; accepted 12 December 2017; published online 27 December 2017)

Layered tin sulfide semiconductors are both of fundamental interest and attractive for energy conversion applications. Sn sulfides crystallize in several stable bulk phases with different Sn:S ratios ( $\text{SnS}_2$ ,  $\text{Sn}_2\text{S}_3$ , and  $\text{SnS}$ ), which can transform into phases with a lower sulfur concentration by introduction of sulfur vacancies ( $V_S$ ). How this complex behavior affects the optoelectronic properties remains largely unknown but is of key importance for understanding light-matter interactions in this family of layered materials. Here, we use the capability to induce  $V_S$  and drive a transformation between few-layer  $\text{SnS}_2$  and  $\text{SnS}$  by electron beam irradiation, combined with *in-situ* cathodoluminescence spectroscopy and *ab-initio* calculations to probe the role of defects in the luminescence of these materials. In addition to the characteristic band-edge emission of the endpoint structures, our results show emerging luminescence features accompanying the  $\text{SnS}_2$  to  $\text{SnS}$  transformation. Comparison with calculations indicates that the most prominent emission in  $\text{SnS}_2$  with sulfur vacancies is not due to luminescence from a defect level but involves recombination of excitons bound to neutral  $V_S$  in  $\text{SnS}_2$ . These findings provide insight into the intrinsic and defect-related optoelectronic properties of Sn chalcogenide semiconductors. *Published by AIP Publishing.* <https://doi.org/10.1063/1.5007060>

Layered group IV chalcogenide semiconductors have attracted significant interest as electronic materials due to their unique physical properties and potential applications in renewable energy conversion. Tin disulfide ( $\text{SnS}_2$ ) and disulfide/diselenide alloys have been fabricated into field-effect transistors with a high on-off current ratio and carrier mobility comparable to those of transition metal dichalcogenides.<sup>1–4</sup> Other characteristics of these systems such as a bandgap of  $\sim 2.3$  eV for  $\text{SnS}_2$  and suitably aligned redox potentials make them interesting for photocatalysis.<sup>5,6</sup> Tin sulfide ( $\text{SnS}$ ) has shown promise as a photovoltaics absorber material,<sup>7,8</sup> while tin selenide ( $\text{SnSe}$ ) has demonstrated exceptional thermoelectric properties.<sup>9</sup> Finally, monochalcogenides are predicted to be ferroelectrics/multiferroics with substantially smaller bandgaps than typical oxide ferroelectrics,<sup>10,11</sup> which is both of fundamental interest and may enable the realization of 3rd generation solar cell concepts such as shift current photovoltaics.<sup>12,13</sup>

Most of the potential applications take advantage of the optoelectronic properties of tin chalcogenides, which have been determined to date for single crystals,<sup>5,14–17</sup> polycrystalline thin films,<sup>18–20</sup> or chemically synthesized nanoflakes.<sup>21</sup> The fact that Sn chalcogenides can exist in three different bulk crystal structures with different chalcogen contents (e.g.,  $\text{SnS}_2$ ,  $\text{Sn}_2\text{S}_3$ , and  $\text{SnS}$ ) not only makes these materials interesting but also causes complications: The absence of a fixed stoichiometry implies that several phases may be present both

in source materials (precursor powders, evaporation materials, and sputtering targets) and in the resulting films.<sup>8,22</sup> Sousa *et al.* recently suggested thermal annealing of sputtered  $\text{SnS}_2$  films as a possible route toward single-phase  $\text{SnS}$  for photovoltaics,<sup>23</sup> using the fact that the composition can be continuously varied across the entire spectrum of materials via introduction of defects such as sulfur vacancies ( $V_S$ ). Such defects, which are likely to be abundant as they can be produced in material synthesis as well as during thermal processing or by interaction with energetic electron or ion beams, can strongly affect light absorption and emission. Several theoretical studies have addressed the defect chemistry, e.g., the formation energy of different defects in  $\text{SnS}$ <sup>24</sup> and across all three stable phases of the Sn-sulfide family.<sup>25</sup> In experiments, few efforts have been made to control the concentration of defects and identify the link between defects or the resulting bandgap states and their optoelectronic properties. Thus, the precise relationship between the features in the optical spectra and defect types remains poorly understood. Here, we use controlled structural transformations between  $\text{SnS}_2$  and  $\text{SnS}$  by generating abundant  $V_S$  during exposure to a high-energy electron beam,<sup>26</sup> along with high spatial resolution cathodoluminescence spectroscopy in scanning transmission electron microscopy (STEM-CL) and *ab-initio* calculations to study the optoelectronic signatures of different Sn sulfide phases and of their defects. Our results indicate a rich set of optically active defect states appearing during the transformation from  $\text{SnS}_2$  to  $\text{SnS}$ .

<sup>a)</sup>Author to whom correspondence should be addressed: psutter@unl.edu.

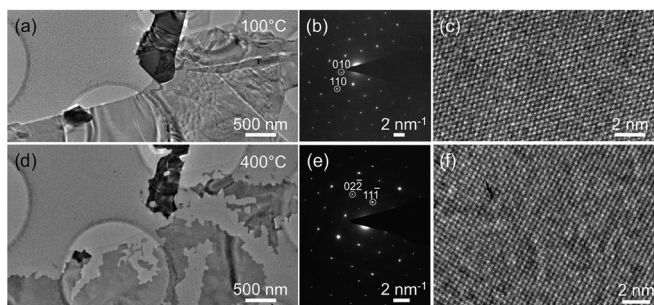


FIG. 1. Electron-beam induced transformation of few-layer  $\text{SnS}_2$  to  $\text{SnS}$  at elevated temperatures. (a) TEM image of  $\text{SnS}_2$  flakes at  $100^\circ\text{C}$  at the initial stages of the electron-beam induced transformation. (b) Electron diffraction pattern showing pure trigonal  $\text{SnS}_2$  along the  $[001]$  zone axis (ZA, equivalent to  $[0001]$  in Bravais-Miller 4 index notation). Similarly, the  $(010)$  plane is identical to the  $(01\bar{1}0)$  plane and the  $(110)$  plane to the  $(11\bar{2}0)$  plane. (c) HRTEM lattice image of the starting material, showing the characteristic 6-fold symmetry of layered  $\text{SnS}_2$ .<sup>1</sup> (d) TEM image of the same region shown in (a) after exposure to the electron beam at  $400^\circ\text{C}$ , which causes a transformation to uniform  $\text{SnS}$  over large areas along with an overall loss of material. (e) Electron diffraction pattern showing the pure orthorhombic  $\alpha$ - $\text{SnS}$  crystal structure along the  $[011]$  ZA. (f) HRTEM lattice image of the transformed flake, showing the orthorhombic structure of few-layer  $\text{SnS}$ .

Experiments were carried out on few-layer  $\text{SnS}_2$  flakes, mechanically exfoliated to below 10 layer thickness from high-quality, Cl-doped single crystals grown by the vertical Bridgman method<sup>27</sup> and supported on transmission electron microscopy (TEM) grids with amorphous carbon membranes. Electron-beam-induced structural transformations were performed in an FEI Osiris ChemiSTEM at a beam energy of 200 keV, with samples heated to  $400^\circ\text{C}$  on a Gatan 652 high-temperature sample holder to achieve larger areas (up to  $\sim 1 \mu\text{m}^2$ ) of transformed materials. In addition to  $\text{SnS}_2$ , reference samples of nominally pure  $\text{SnS}$  powder [Tin (II) sulfide, 96%; Sigma Aldrich] were prepared by ultrasonication of the powder in de-ionized water, followed by drop-casting on carbon membrane TEM grids. Optoelectronic properties were assessed at room temperature and 110 K by STEM-CL, measured using a Gatan Vulcan STEM-CL system on a FEI Osiris instrument and on a FEI Talos field-emission (S)TEM at a primary electron energy of 200 keV and a typical beam current of 250 pA. The typical spatial resolution in these measurements is illustrated in Fig. S1, [supplementary material](#). Complementary measurements included micro-Raman spectroscopy, performed on a Horiba Xplora Plus instrument with an excitation wavelength of 532 nm at a power of  $\sim 16 \mu\text{W}$ .

Electronic band structures were calculated within the framework of density functional theory (DFT), carried out in the plane-wave basis and within the projector-augmented wave (PAW) description of the core regions, as implemented in VASP.<sup>28,29</sup> We adopted a plane wave cutoff of 500 eV and k-point meshes of  $12 \times 12 \times 6$  for  $\text{SnS}_2$  and  $12 \times 12 \times 4$  for  $\text{SnS}$ . In hybrid functional calculations, the k-point mesh in the Fock exchange operator was halved. In order to reproduce the experimental lattice parameters and bandgaps of  $\text{SnS}_2$ , we benchmarked four exchange-correlation functionals: PBE, PBE-D2, revB86b, and HSE-D2.<sup>30–33</sup> While the functional with van der Waals interactions yielded a good  $c$  lattice parameter, all functionals with semilocal exchange gave too large lattice constant  $a$ . Only the HSE functional with vdW interactions accounted for empirically at the D2 level

provided a good description of both parameters (see [supplementary material](#)). In addition, semilocal functionals significantly underestimated the bandgap, whereas HSE slightly overestimated it. For a more straightforward comparison with experiment, the fraction of the exact exchange was reduced to 0.22 from the standard value of 0.25, whereby the calculated gap (without excitonic effects) reproduces the experimental gap (with excitonic effects). This is justified by the small exciton binding energy of 0.1 eV in bulk  $\text{SnS}_2$ .<sup>34</sup> The lattice constants were largely unaffected by this change. The same functional was also used for  $\text{SnS}$ , yielding good lattice parameters and bandgaps. In considering the properties of defects in  $\text{SnS}_2$ , we focused on sulfur vacancies ( $V_S$ ) and chlorine dopants substituted in the S sites. Calculations were carried out in a  $5 \times 5 \times 3$  supercell (225 atoms). We used a cut-off energy of 300 eV and a  $2 \times 2 \times 2$  k-point mesh. Fock exchange was evaluated solely at the  $\Gamma$  point. Since the binding energy of bound excitons can be larger than that of free excitons, we have probed these electron-hole interactions by carrying out  $\Delta\text{SCF}$  calculations with fixed state occupations (see [supplementary material](#), Note 1).

Figure 1 shows the effects of electron-beam irradiation at elevated temperatures on the morphology and atomic structure of few-layer  $\text{SnS}_2$ . In TEM, the starting material—thin  $\text{SnS}_2$  flakes exfoliated from a crystal of the layered material<sup>35</sup>—is imaged as extended domains with few  $\mu\text{m}$  lateral dimensions and a largely uniform thickness [Fig. 1(a)]. Networks of wrinkles exist in these flakes, mostly in areas supported by the carbon membrane of the TEM grid. Some thicker areas [e.g., top center of Fig. 1(a)] are identified via their darker (mass-thickness) contrast. Electron diffraction shows the characteristic sixfold symmetric pattern of rhombohedral  $\text{SnS}_2$  [Fig. 1(b)]. No other crystalline phases are detectable. Consistent with the diffraction results, high-resolution TEM (HRTEM) shows a well-ordered lattice with contrast and lattice parameter characteristic of layered  $\text{SnS}_2$  imaged along the  $c$ -axis (i.e., perpendicular to the plane of the covalently bonded layers).<sup>1,26</sup> In previous work, we showed that electron-beam irradiation of  $\text{SnS}(\text{e})_2$  induces chalcogen vacancies, followed by ordering into vacancy lines and ultimately a complete transformation into the less chalcogen-containing phase  $\text{SnS}(\text{e})$ .<sup>26</sup>

Whereas at room temperature this transformation produces small, few-nm scale single crystal areas of the final phase embedded in the parent  $\text{SnS}(\text{e})_2$  crystal, at elevated temperatures, large areas can be transformed uniformly by electron-beam irradiation. This is documented in Fig. 1(d)–1(f). Figure 1(d) shows a TEM image of the same flake shown in Fig. 1(a) after exposure to 200 keV electrons at  $400^\circ\text{C}$ . In thin areas, clear signs of the effects of this processing can be seen, notably the opening of voids in the previously continuous flake. A majority of these voids are bound by straight, faceted edges, most of which enclose  $90^\circ$  angles with each other. The mass loss that gives rise to these voids likely involves sublimation of the final  $\text{SnS}$  phase at the elevated temperatures of our experiments, possibly assisted by additional energy transfer from the electron beam. Electron diffraction across both larger ( $>1 \mu\text{m}$ ) and smaller continuous flake segments shows a pattern that can be indexed to orthorhombic  $\text{SnS}$  [Fig. 1(e)]. The  $\text{SnS}$  layers are no longer stacked along the surface normal but are tilted  $\sim 21^\circ$  relative

to the plane of the original SnS<sub>2</sub> trilayers as determined from the diffraction patterns and HRTEM images that are oriented such that the electron beam projects along the [011] direction.<sup>26</sup> Again, no secondary crystalline phases are detectable, and the contrast in HRTEM is consistent with the transformation of the entire area of SnS<sub>2</sub> into SnS [Fig. 1(f)].

The electron-beam induced removal of S-atoms from well-ordered SnS<sub>2</sub> crystals, i.e., generation of V<sub>S</sub> ultimately followed by a structural transformation to SnS, presents a unique opportunity for identifying optoelectronic signatures not only of the two endpoint structures SnS<sub>2</sub> and SnS but also of defective intermediates between these phases, e.g., SnS<sub>2</sub> with an increasing density of V<sub>S</sub>. To gather such information, we used *in-situ* spectroscopy in STEM-CL, which enables measurements of luminescence spectra with excitation by a focused electron beam rather than optical (laser) excitation and thus provides optoelectronic information at length scales far below the diffraction limit of conventional photoluminescence (PL) spectroscopy.<sup>36</sup> In Fig. 2, this capability is used to probe luminescence from SnS<sub>2</sub> at different stages of the electron-beam induced transformation to SnS. Figures 2(a) and 2(b) show high-angle annular dark-field STEM (HAADF-STEM) images of typical SnS<sub>2</sub> flakes, obtained with minimal electron exposure [Fig. 2(a)] and after extended exposure at elevated temperature [Fig. 2(b)], respectively. Figure 2(c) displays the corresponding CL spectra. Note that the SnS<sub>2</sub> crystal shown in Fig. 2(b) has varying thicknesses and that thicker areas (with brighter HAADF-STEM contrast) are less affected by electron irradiation at the same dose. Hence, thickness variations can be leveraged to survey and compare luminescence at different stages of the transformation on a single flake.

The CL spectrum measured for SnS<sub>2</sub> with minimal electron exposure [Fig. 2(c-i)] shows a broad emission maximum between  $\sim 1.8$  and 2.4 eV, i.e., in a spectral region that includes the reported indirect gap of SnS<sub>2</sub> ( $\sim 2.3$  eV at 110 K),<sup>5</sup> but which already extends into the bandgap as well.

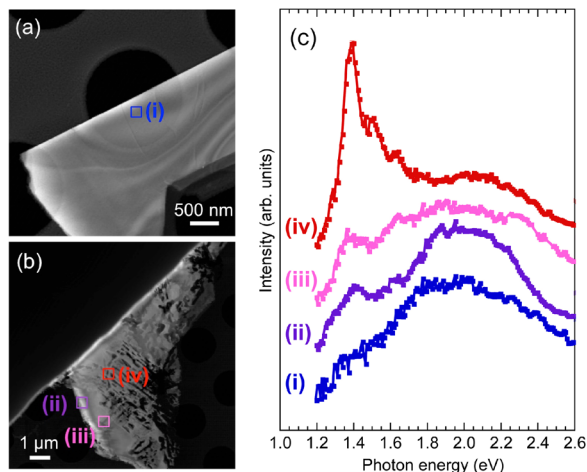


FIG. 2. Cathodoluminescence (CL) spectra of SnS<sub>2</sub> transformed by electron-beam irradiation. (a) and (b) HAADF-STEM images of SnS flakes at early (a) and late stages (b) of electron-beam induced transformation at 400 °C. (c) CL spectra showing the progression of luminescence with the transformation from SnS<sub>2</sub> to SnS (400 °C). Spectra (i)–(iv) are measured at locations marked in (a) and (b). Spectra obtained at T = 110 K using 200 keV focused electron beam excitation in STEM.

Thinner areas with more advanced transformation show an increase in the intensity of the sub-bandgap emission, first centered at  $\sim 2.0$  eV [Fig. 2(c-ii)] and then to lower photon energies. In addition, a well-defined peak begins to emerge, which is centered at 1.40 eV. In the thinnest (i.e., most transformed) areas, this additional luminescence feature ultimately emerges as a sharp, intense peak at 1.38 eV with a shoulder toward higher photon energies [1.4–1.8 eV; Fig. 2(c-iv)].

In thin SnS<sub>2</sub> areas as shown in Fig. 2, the luminescence within the SnS<sub>2</sub> bandgap is rather broad and shows no distinct spectral features except for the emerging peak at  $\sim 1.40$  eV. To probe in more detail possible defect-mediated luminescence due to the formation of V<sub>S</sub>, we measured CL spectra on thicker SnS<sub>2</sub> flakes along with reference samples extracted from nominally pure SnS powder (also see the Raman spectrum, Fig. S2, [supplementary material](#)). These measurements are shown in Fig. 3 along with calculated band structures of SnS<sub>2</sub> and SnS to illustrate the main optical transitions in defect-free crystals.

We first discuss the CL spectra obtained on the SnS reference samples. The spectrum in Fig. 3(c) shows a luminescence feature near 1.4 eV, which can be deconvoluted into three individual Gaussian peaks centered at 1.25 eV, 1.36 eV, and 1.48 eV. Comparison with the computed band structure of SnS [Fig. 3(f)] and with absorption measurements for SnS<sup>19,23,37</sup> leads us to assign the lower energy peaks to radiative recombination across the indirect and direct bandgaps of SnS, respectively. In some instances, more complex spectra are observed for the same powders [Fig. 3(d)], with additional peaks emerging at both lower ( $\sim 1.2$  eV) and higher (up to  $\sim 1.8$  eV) photon energies. Given that the simplest spectra comprise fewer peaks around 1.4 eV, we assign these

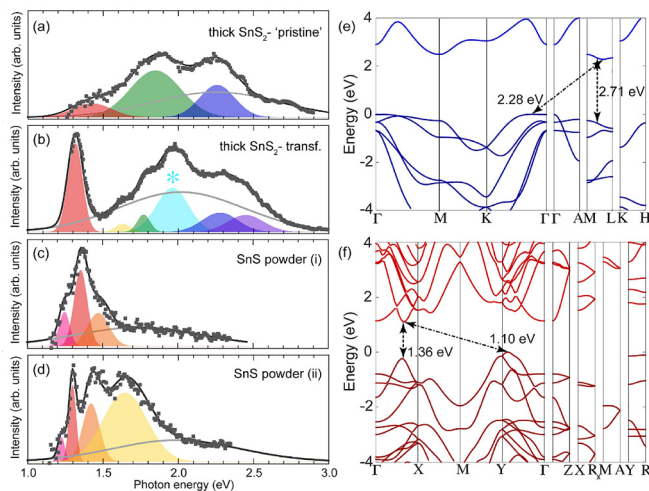


FIG. 3. Optoelectronic signatures in cathodoluminescence spectra of nearly pristine and partially transformed, thicker tin disulfide (SnS<sub>2</sub>) and a tin monosulfide (SnS) powder reference. (a) CL spectrum measured on thick SnS<sub>2</sub> after minimal exposure to 200 keV electrons. (b) CL spectrum of thick SnS<sub>2</sub> after longer exposure to high-energy electrons to induce loss of sulfur. (c) and (d) Two types of spectra observed for nominally SnS powder. Spectra obtained at 110 K (b) and room temperature (a), (c), and (d), respectively, using 200 keV electron excitation in STEM. Symbols: measured spectra. Colored areas: Gaussian fits to the data. Light gray lines: Gaussian fits to the signal background, in lieu of a background subtraction. (e) and (f)  $\Gamma=0$  band structure of (e) SnS<sub>2</sub> and (f) SnS calculated with HSE(0.22)-D2. Arrows denote the direct and indirect bandgaps. Energy zero is set at the valence band (VB) maximum.

additional luminescence features to the coexistence of other phases in the nominally pure SnS powders, as reported previously.<sup>8,22</sup> Based on these reference measurements, the luminescence developing near 1.4 eV at later stages of electron-beam irradiation of SnS<sub>2</sub> can be ascribed to band-to-band transitions in increasing amounts of the final SnS phase.

CL spectroscopy on electron irradiated thicker SnS<sub>2</sub> flakes has been used to obtain clearer spectral signatures of defective SnS<sub>2</sub> at early and intermediate stages of the transformation to SnS than that could be detected in thin, few-layer SnS<sub>2</sub>. Examples of such measurements are shown in Figs. 3(a) and 3(b). The early stage spectrum [Fig. 3(a)] shows the characteristic band-edge emission of SnS<sub>2</sub> (2.26 eV), a weak broader peak originating from small amounts of SnS (1.4 eV), and an as yet unidentified feature centered at 1.84 eV. The spectrum at a more advanced stage of the electron-beam induced transformation [Fig. 3(b)] comprises two families of features: An intense, narrow (full-width at half maximum, FWHM  $\sim 0.1$  eV) peak centered at 1.32 eV, close to the features observed in late-stage transformed thin SnS<sub>2</sub> [Fig. 2(c-iv)] and in the SnS reference Fig. 3(c); and a broad-band emission (1.5–2.7 eV) that clearly contains several discrete contributions. We performed a lineshape analysis with a minimal number of Gaussian components to fit this broad emission peak. On the high-energy side, the analysis identifies two components at 2.28 eV and 2.45 eV, which by comparison with calculations [Fig. 3(e)] and absorption data<sup>5</sup> are ascribed to transitions across the indirect and direct bandgap of SnS<sub>2</sub>, respectively. On the low-energy side, we find two weak components that may be associated with the final SnS phase or intermediate minority phases, both of which show luminescence in this range [Figs. 3(b) and 3(c)]. The dominant feature in the thick, defective SnS<sub>2</sub>, however, is a somewhat broader (FWHM  $\sim 0.25$  eV) luminescence peak centered at a photon energy of 1.96 eV [marked by \* in Fig. 3(b)]. The intensity and energy of this peak—near the conduction band minimum of SnS<sub>2</sub> and much higher than any of the emission features due to SnS—suggest that it is due to lattice defects (i.e., V<sub>S</sub>) induced by the electron irradiation of SnS<sub>2</sub>.

*Ab-initio* calculations were carried out to further substantiate this assignment and identify the nature of the presumed defect emission. The results of these calculations are summarized in Fig. 4 (see [supplementary material](#) for further details). PBE and HSE(0.22)-D2 formation energy diagrams for sulfur vacancies are shown in Fig. S3 ([supplementary material](#)). In the neutral charge state, the defect shows a doubly occupied state in the gap. The stable charge states are +2, +1, and 0, where +2/+1 and +1/0 transition levels lie close to each other. The charge transition levels are in fair agreement with the values reported recently.<sup>25</sup> Fig. S3 ([supplementary material](#)) also shows a configuration coordinate representation of the transition between different charge states, which was used to estimate the energies of optical transitions involving the V<sub>S</sub> defect level without excitonic effects. The calculated value for absorption is 1.88 eV and for emission is 0.74 eV. The latter is below the acceptance window of our STEM-CL system, and its experimental verification would require near-infrared CL or PL, which is not available to us. Relaxation has a strong effect on the energies and is reflected in sizable changes to the defect geometry. This might lead to efficient non-radiative

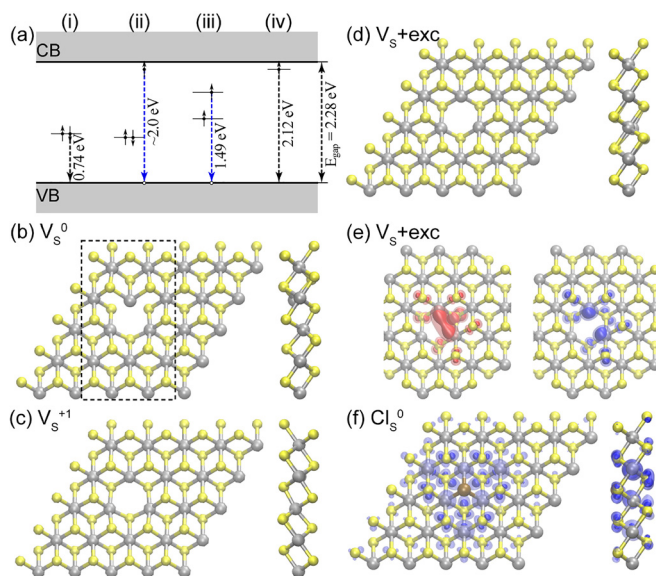


FIG. 4. Radiative transitions in defective SnS<sub>2</sub>. (a) Computed recombination energies for different transitions: (i) V<sub>S</sub> defect level to valence band (VB); (ii) Exciton bound to neutral V<sub>S</sub><sup>0</sup>; (iii) Exciton bound to charged V<sub>S</sub><sup>+</sup>; (iv) Cl<sub>S</sub> defect level to VB. Relaxed structures of (b) V<sub>S</sub><sup>0</sup>; (c) V<sub>S</sub><sup>+</sup>; (d) V<sub>S</sub> + exciton. Partial charge density of the defect states of (e) V<sub>S</sub> + exciton; (f) Cl<sub>S</sub> defect state.

recombination. As can be seen in Fig. 4(b), in the neutral charge state (V<sub>S</sub><sup>0</sup>), one of the Sn atoms is displaced out of the metal plane. The length of the “broken bond” is 2.92 Å (with a back bond of 2.70 Å), in comparison with the bulk value of 2.56 Å. In the V<sub>S</sub><sup>+</sup> state, these values decrease to 2.66 Å (2.53 Å).

It was assumed in the above calculations that the electrons/holes on the band edges are free and have the energy of the CBM/VBM far from the defect. Going beyond this picture, we can approximately take into account possible emission from bound excitons by forcing extra electrons/holes to the CBM/VBM states (see [supplementary material](#) Note 1 for details). The most important optical (emission) transitions are summarized in Fig. 4(a). Case (i) is the defect-mediated transition considered above (no excitonic transition). Case (ii) involves a neutral vacancy, with electrons at CBM and holes at VBM. The binding energy of the exciton (whose magnitude can be estimated from the binding energy of the free exciton in bulk SnS<sub>2</sub>,  $\sim 0.1$  eV)<sup>34</sup> and the binding to the defect are quite small, and the resulting optical emission due to recombination of the bound exciton is around 2.0 eV. Case (iii) is the same for the vacancy in the +1 charge state. Here, the extra electron in the conduction band localizes near the defect, essentially yielding a neutral defect with a magnetic moment of  $2 \mu_B$ , whereas the hole is not localized due to repulsion from the defect. The emission for this case is at  $\sim 1.5$  eV. We also considered possible transitions involving Cl-dopants substitutional in S sites (see Fig. S4, [supplementary material](#)) and found a transition close to the SnS<sub>2</sub> bandgap at 2.12 eV [Fig. 4(a-iv)], for both the defect-mediated transition and the “bound exciton” state (see [supplementary material](#)).

Comparing the calculated optical transitions with experiment, we find good agreement between the computed “bound exciton” related emissions [Figs. 4(a-ii) and 4(a-iii)] and peaks found in STEM-CL [Fig. 3(b)]. Whereas the measured intensity near 1.5 eV (i.e., emission via a possible (charged) V<sub>S</sub><sup>+</sup>

bound exciton) is low and could also be attributed to transitions in SnS [compare Figs. 3(c) and 3(d)], the intense peak at 1.96 eV is unique to defective SnS<sub>2</sub> with a large density of V<sub>S</sub>. The energy of this peak is close to the computed value of 2.0 eV, and hence, we assign it to emission involving a (neutral) V<sub>S</sub><sup>0</sup> bound exciton in sulfur-deficient SnS<sub>2</sub>. The broadness of this peak could reflect modifications to the defect states when vacancies interact with each other and finally agglomerate into lines at larger concentrations, as proposed in Ref. 26. In addition, transitions related to Cl-dopants can contribute to the high-energy tail of the peak.

In conclusion, we have used STEM-CL combined with DFT to probe luminescence in tin chalcogenide semiconductors, a group of layered materials with optoelectronic properties of interest for energy conversion processes including photovoltaics and photocatalysis. The experiments took advantage of the ability to generate sulfur vacancies in tin disulfide by high-energy electron irradiation, which at elevated temperatures ultimately leads to the complete transformation to tin monosulfide. Using this effect, different amounts of sulfur vacancies could be induced *in-situ* (in the electron microscope) followed by STEM-CL spectroscopy of radiative recombination in these defective materials. Applied to thin SnS<sub>2</sub>, this approach shows clear signatures of the end-point structures SnS<sub>2</sub> and SnS, but the spectral features in the transition regime (i.e., for defective SnS<sub>2</sub>) are broad. Measurements on thicker SnS<sub>2</sub>, combined with spectra for a SnS powder reference, give narrower luminescence peaks that can be compared with theoretical calculations. Such comparison identifies a dominant emission in the visible region near a photon energy of 2.0 eV as recombination of excitons bound to neutral sulfur vacancies in defective SnS<sub>2</sub>. Given the increasing importance of tin sulfides for energy applications and the complexity of this material system—with three stable bulk phases (SnS<sub>2</sub>, Sn<sub>2</sub>S<sub>3</sub>, and SnS)<sup>16</sup> and the possibility of continuously varying the composition via introduction of sulfur vacancies—our results provide important spectroscopic signatures as a basis for tuning tin sulfides for optoelectronic applications.

See [supplementary material](#) for calculated lattice constants and bandgaps of SnS<sub>2</sub> and SnS (supplementary tables); CL and Raman spectroscopy and computed formation energy diagrams for the S vacancy and the Cl dopant in SnS<sub>2</sub> (supplementary figures); computational details (supplementary notes); Supplementary references.

This work was supported by the U.S. Department of Energy, Office of Science, Basic Energy Sciences, under Award No. DE-SC0016343. For the theoretical calculations, A.V.K. and H.P.K. acknowledge the Academy of Finland for support under Project No. 286279, the support from the U.S. Army RDECOM via Contract No. W911NF-15-1-0606, and the support of the Ministry of Education and Science of the Russian Federation in the framework of Increase Competitiveness Program of NUST «MISiS» (No. K3-2017-021). We also thank the CSC-IT Center for Science Ltd. for generous grants of computer time.

- <sup>1</sup>Y. Huang, E. Sutter, J. T. Sadowski, M. Cotlet, O. L. A. Monti, D. A. Racke, M. R. Neupane, D. Wickramaratne, R. K. Lake, B. A. Parkinson, and P. Sutter, *ACS Nano* **8**(10), 10743–10755 (2014).
- <sup>2</sup>T. S. Pan, D. De, J. Manongdo, A. M. Guloy, V. G. Hadjiev, Y. Lin, and H. B. Peng, *Appl. Phys. Lett.* **103**(9), 093108 (2013).
- <sup>3</sup>H. S. Song, S. L. Li, L. Gao, Y. Xu, K. Ueno, J. Tang, Y. B. Cheng, and K. Tsukagoshi, *Nanoscale* **5**(20), 9666–9670 (2013).
- <sup>4</sup>D. Debtanu, M. John, S. Sean, Z. Vincent, G. Arnold, and P. Haibing, *Nanotechnology* **24**(2), 025202 (2013).
- <sup>5</sup>L. A. Burton, T. J. Whittles, D. Hesp, W. M. Linhart, J. M. Skelton, B. Hou, R. F. Webster, G. O'Dowd, C. Reece, D. Cherns, D. J. Fermin, T. D. Veal, V. R. Dhanak, and A. Walsh, *J. Mater. Chem. A* **4**(4), 1312–1318 (2016).
- <sup>6</sup>Y. Sun, H. Cheng, S. Gao, Z. Sun, Q. Liu, Q. Liu, F. Lei, T. Yao, J. He, S. Wei, and Y. Xie, *Angew. Chem. Int. Ed.* **51**(35), 8727–8731 (2012).
- <sup>7</sup>P. Sinsermsuksakul, L. Sun, S. W. Lee, H. H. Park, S. B. Kim, C. Yang, and R. G. Gordon, *Adv. Energy Mater.* **4**(15), 1400496 (2014).
- <sup>8</sup>V. Steinmann, R. Jaramillo, K. Hartman, R. Chakraborty, R. E. Brandt, J. R. Poindexter, Y. S. Lee, L. Sun, A. Polizzotti, H. H. Park, R. G. Gordon, and T. Buonassisi, *Adv. Mater.* **26**(44), 7488–7492 (2014).
- <sup>9</sup>L.-D. Zhao, S.-H. Lo, Y. Zhang, H. Sun, G. Tan, C. Uher, C. Wolverton, V. P. Dravid, and M. G. Kanatzidis, *Nature* **508**(7496), 373–377 (2014).
- <sup>10</sup>R. Fei, W. Li, J. Li, and L. Yang, *Appl. Phys. Lett.* **107**(17), 173104 (2015).
- <sup>11</sup>M. Wu and X. C. Zeng, *Nano Lett.* **16**(5), 3236–3241 (2016).
- <sup>12</sup>A. M. M. Cook, B. Fregoso, F. de Juan, S. Coh, and J. E. Moore, *Nat. Commun.* **8**, 14176 (2017).
- <sup>13</sup>K. Kushnir, M. Wang, P. D. Fitzgerald, K. J. Koski, and L. V. Titova, *ACS Energy Lett.* **2**(6), 1429–1434 (2017).
- <sup>14</sup>T. Shibata, N. Kambe, Y. Muranushi, T. Miura, and T. Kishi, *J. Phys. D: Appl. Phys.* **23**(6), 719 (1990).
- <sup>15</sup>B. F. Bilenkii, A. G. Mikolaichuk, and D. M. Freik, *Phys. Status Solidi (b)* **28**(1), K5–K7 (1968).
- <sup>16</sup>L. A. Burton, D. Colombara, R. D. Abellon, F. C. Grozema, L. M. Peter, T. J. Savenije, G. Dennler, and A. Walsh, *Chem. Mater.* **25**(24), 4908–4916 (2013).
- <sup>17</sup>T. Raadik, M. Grossberg, J. Raudoja, R. Traksmaa, and J. Krustok, *J. Phys. Chem. Solids* **74**(12), 1683–1685 (2013).
- <sup>18</sup>J. George and K. S. Joseph, *J. Phys. D: Appl. Phys.* **15**(6), 1109 (1982).
- <sup>19</sup>Y. Kawano, J. Chantana, and T. Minemoto, *Curr. Appl. Phys.* **15**(8), 897–901 (2015).
- <sup>20</sup>P. Sinsermsuksakul, J. Heo, W. Noh, A. S. Hock, and R. G. Gordon, *Adv. Energy Mater.* **1**(6), 1116–1125 (2011).
- <sup>21</sup>A. J. Bicchieri, D. D. Vaughn, and R. E. Schaak, *J. Am. Chem. Soc.* **135**(31), 11634–11644 (2013).
- <sup>22</sup>A. Wangperawong, S. M. Herron, R. R. Runser, C. Hägglund, J. T. Tanskanen, H.-B.-R. Lee, B. M. Clemens, and S. F. Bent, *Appl. Phys. Lett.* **103**(5), 052105 (2013).
- <sup>23</sup>M. G. Sousa, A. F. da Cunha, and P. A. Fernandes, *J. Alloys Compd.* **592**, 80–85 (2014).
- <sup>24</sup>B. D. Malone, A. Gali, and E. Kaxiras, *Phys. Chem. Chem. Phys.* **16**(47), 26176–26183 (2014).
- <sup>25</sup>Y. Kumagai, L. A. Burton, A. Walsh, and F. Oba, *Phys. Rev. Appl.* **6**(1), 014009 (2016).
- <sup>26</sup>E. Sutter, Y. Huang, H. P. Komsa, M. Ghorbani-Asl, A. V. Krasheninnikov, and P. Sutter, *Nano Lett.* **16**(7), 4410–4416 (2016).
- <sup>27</sup>L. Sharp, D. Soltz, and B. A. Parkinson, *Cryst. Growth Des.* **6**(6), 1523–1527 (2006).
- <sup>28</sup>G. Kresse and J. Hafner, *Phys. Rev. B* **47**(1), 558–561 (1993).
- <sup>29</sup>G. Kresse and J. Furthmüller, *Comput. Mater. Sci.* **6**(1), 15–50 (1996).
- <sup>30</sup>J. P. Perdew, K. Burke, and M. Ernzerhof, *Phys. Rev. Lett.* **77**(18), 3865–3868 (1996).
- <sup>31</sup>S. Grimme, *J. Comput. Chem.* **27**(15), 1787–1799 (2006).
- <sup>32</sup>J. Heyd, G. E. Scuseria, and M. Ernzerhof, *J. Chem. Phys.* **118**(18), 8207–8215 (2003).
- <sup>33</sup>J. Heyd, G. E. Scuseria, and M. Ernzerhof, *J. Chem. Phys.* **124**(21), 219906 (2006).
- <sup>34</sup>J. M. Gonzalez and I. I. Oleynik, *Phys. Rev. B* **94**(12), 125443 (2016).
- <sup>35</sup>Y. Huang, E. Sutter, N. N. Shi, J. Zheng, T. Yang, D. Englund, H.-J. Gao, and P. Sutter, *ACS Nano* **9**(11), 10612–10620 (2015).
- <sup>36</sup>Z. Mahfoud, A. T. Dijkstra, C. Javaux, P. Bassoul, A.-L. Baudrion, J. Plain, B. Dubertret, and M. Kociak, *J. Phys. Chem. Lett.* **4**(23), 4090–4094 (2013).
- <sup>37</sup>K. Hartman, J. L. Johnson, M. I. Bertoni, D. Reicht, M. J. Aziz, M. A. Scarpulla, and T. Buonassisi, *Thin Solid Films* **519**(21), 7421–7424 (2011).